

Bifurcation analysis of visual angle model with anticipated time and stabilizing driving behavior

Xueyi Guan(管学义), Rongjun Cheng(程荣军), and Hongxia Ge(葛红霞)
Citation: Chin. Phys. B, 2022, 31 (**7**): 070507. DOI: 10.1088/1674-1056/ac5606
Journal homepage: http://cpb.iphy.ac.cn; http://iopscience.iop.org/cpb

What follows is a list of articles you may be interested in

Stabilization strategy of a car-following model with multiple time delays of the drivers

Weilin Ren(任卫林), Rongjun Cheng(程荣军), and Hongxia Ge(葛红霞)
Chin. Phys. B, 2021, 30 (**12**): 120506. DOI: 10.1088/1674-1056/abfcc9

A novel class of two-dimensional chaotic maps with infinitely many coexisting attractors

Li-Ping Zhang(张丽萍), Yang Liu(刘洋), Zhou-Chao Wei(魏周超), Hai-Bo Jiang(姜海波), Qin-Sheng Bi(毕勤胜)
Chin. Phys. B, 2020, 29 (**6**): 060501. DOI: 10.1088/1674-1056/ab8626

Effect of magnetic flow and external forcing current on mixed bursting in the pre-Bötzinger complex

Dou-Dou Guo(郭豆豆), Zhuo-Sheng Lü(吕卓生)
Chin. Phys. B, 2019, 28 (**11**): 110501. DOI: 10.1088/1674-1056/ab43b9

Multi-stability involved mixed bursting within the coupled pre-Bötzinger complex neurons

Zijian Wang(王子剑), Lixia Duan(段利霞), Qinyu Cao(曹秦禹)
Chin. Phys. B, 2018, 27 (**7**): 070502. DOI: 10.1088/1674-1056/27/7/070502

Bifurcation analysis of the logistic map via two periodic impulsive forces

Jiang Hai-Bo, Li Tao, Zeng Xiao-Liang, Zhang Li-Ping
Chin. Phys. B, 2014, 23 (**1**): 010501. DOI: 10.1088/1674-1056/23/1/010501

Bifurcation analysis of visual angle model with anticipated time and stabilizing driving behavior

Xueyi Guan(管学义), Rongjun Cheng(程荣军)†, and Hongxia Ge(葛红霞)

Faculty of Maritime and Transportation, Ningbo University, Ningbo 315211, *China*

(Received 6 December 2021; revised manuscript received 22 January 2022; accepted manuscript online 17 February 2022)

In the light of the visual angle model (VAM), an improved car-following model considering driver's visual angle, anticipated time and stabilizing driving behavior is proposed so as to investigate how the driver's behavior factors affect the stability of the traffic flow. Based on the model, linear stability analysis is performed together with bifurcation analysis, whose corresponding stability condition is highly fit to the results of the linear analysis. Furthermore, the time-dependent Ginzburg–Landau (TDGL) equation and the modified Korteweg–de Vries (mKdV) equation are derived by nonlinear analysis, and we obtain the relationship of the two equations through the comparison. Finally, parameter calibration and numerical simulation are conducted to verify the validity of the theoretical analysis, whose results are highly consistent with the theoretical analysis.

Keywords: visual angle, bifurcation analysis, anticipated time, stabilizing driving behavior, TDGL and mKdV equations

PACS: 05.60.–k, 45.70.Vn **DOI:** 10.1088/1674-1056/ac5606

1. Introduction

In recent years, the demand for transportation has maintained a continuous growth, which has brought huge challenges to the smooth traffic and traffic safety. Facing the traffic problems, numerous of scholars proposed a series of traffic flow models to explain the complex traffic phenomena. These models[1–9] mainly model the traffic flow from three modules: macroscopic, microscopic and mesoscopic. For example, Sun *et al.*[1] proposed a car-following model, one of the microscopic models of vehicular traffic, which is concentrating on individual vehicles, and studying the characteristics of the following vehicles in the entire fleet by studying the influence of the changes in the movement state of the leading vehicle on the following vehicles, meanwhile the theoretical analysis and simulation of the improved model not only can provide deep exploring into the properties of the model but also help in better understanding the complex phenomena observed in real traffic fields. In addition, we can also subdivide these models into the car-following models (e.g., Sun *et al.*,[1] Ge *et al.*[2] and Jiang *et al.*[3]), the cellular automation models (Tian *et al.*[4]), the gas kinetic models (Nagatani *et al.*[5]), the hydrodynamic lattice models (Redhu *et al.*[6] and Chang *et al.*[7]) and the continuum models (Cheng *et al.*[8] and Zhai *et al.*[9]) according to different modeling theories. Bifurcation, as an important research content of non-linear science, mainly studies the instability of the system solution caused by parameter changes and the changing behavior of the number of solutions. Studying the bifurcation in traffic flow will have important theoretical implications in analyzing traffic phenomena, traffic modeling, traffic control, etc.

Facing numerous of traffic congestions, a number of mathematical models have been proposed to demonstrate the car-following behavior under various conditions with the development of urban transportation. Generally speaking, these models are mostly based on the stimulus-response framework, which was put forward at the General Motors research laboratories (Chandler *et al.*[10] and Gazis *et al.*[11]) at the first time. According to the framework, each driver responds when giving a stimulus. And the relationship between response and stimulus is as follows:

$$\text{response} = \text{sensitivity} \times \text{stimulus}.$$

In the framework, the stimulus could be mainly divided into four aspects: driver's behavior factors, vehicle factors, road factors and other factors. However, when it comes to car-following model equation, the stimulus could be related to the location of a large number of cars or their speed, or maybe some other coefficient. The reaction which demonstrates the propulsion of follower has been transformed into vehicle's speeds or accelerations. In different forms of car-following models, the reason for the different forms of vehicle motion equations lies in the different hypotheses of stimulus properties. The stimulus is probably composed of the speed, the speed difference between two consecutive vehicles, the headway, etc. Following are some classic car-following models that consider different stimulus.

Gazis–Herman–Rothery (GHR)[11] car-following model is perhaps the most recognized model in the research of traffic flow, which is the foundation of the car-following model

†Corresponding author. E-mail: chengrongjun@nbu.edu.cn

© 2022 Chinese Physical Society and IOP Publishing Ltd

proposed by Herman *et al.*[12] and Yang *et al.*,[13] displayed as

$$\frac{\mathrm{d}v_n(t)}{\mathrm{d}t} = \lambda \Delta v_n(t-\tau), \tag{1}$$

where λ is the sensitivity of the relative velocity, $\Delta v_n(t-\tau)$ represents the relative velocity of the nth car at time $t-\tau$, τ is reaction time of driver, in addition, and λ has some functional forms as follows:

(a) $\lambda = A$; a constant;

(b) $\lambda = \begin{cases} A_1, & \Delta x_n(t) \le \Delta x_{\text{critical}}(t), \\ A_2, & \Delta x_n(t) > \Delta x_{\text{critical}}(t), \end{cases}$ step function;

(c) $\lambda = A/\Delta x_n(t)$; reciprocal spacing;

(d) $\lambda = A \cdot v_n(t)/\Delta x_n(t)$; referenced by Edie's model (Edie[14]);

(e) $\lambda = A/\Delta x_n(t)^2$ yields Greenshield's (Greenshields *et al.*[15]) macroscopic flow-density relationship;

where $\Delta x_n(t)$ represents distance between two consecutive vehicles, $\Delta x_{\text{critical}}(t)$ is the threshold value obtained from actual data analysis, $v_n(t)$ represents the velocity of nth vehicle, while A, A_1 and A_2 are constant. Moreover, Lee[16] believed that drivers make decisions relying on a period of stimulation rather than a transient stimulus, and for the reason he proposed an improved GM model with considering driver's memory, which is the foundation of the extended car-following model considering driver's memory and jerk proposed by Jin *et al.*[17]

For whether Chandler *et al.*[10] or Gazis *et al.*[11] mentioned earlier, they all assumed that both cars are driving at the same speed and the headway is acceptable, but this is not consistent with the actual situation. To overcome this shortcoming, Newell[18] proposed a nonlinear car-following model by using the headway as a stimulus, and Helly[19] assumed that every driver will adjust the following distance to a desired distance according to his driving characteristics, and drivers strive to minimize the relative speed along with the distance between the actual headway and the required headway, which is defined as

$$a_n(t) = A_1 v_n(t-\tau) + A_2\left(x_n(t-\tau) - D_n(t)\right), \tag{2}$$

where $D_n(t)$ is driver's desired following distance. In view of the earlier work, Helly[19] calculated the final calibration results where $\tau = 0.5$ s, $A_1 = 0.5$ s^{-1}, $A_2 = 0.125$ s^{-2}, and $D_n(t) = 20 + v_n(t-0.5)$. And Helly's improvement also laid the foundation for the innovation of Koshi *et al.*[20] and Xing *et al.*[21] For example, Koshi *et al.*[20] combined Helly's model with GHR's model and did a nonlinear extension, but it still has some shortcomings in horizontal curvature effect.

Then in 1995, Bando[22] proposed the optimal velocity (OV) model, which describes some nonlinear phenomenon and car-following behavior in traffic, and the specific expression shows as following:

$$\frac{\mathrm{d}v_n(t)}{\mathrm{d}t} = \alpha\left[V\left(\Delta x_n(t)\right) - v_n(t)\right], \tag{3}$$

where α donates the coefficient of sensitivity and V represents the optimal velocity that drivers prefer based on the condition of the headway.

Optimal velocity model can reflect some actual traffic flow characteristics such as the disappearance of stability of continuous traffic flow, the queuing of the traffic and the entire process from the generation to the elimination of traffic congestion very well, but when facing high acceleration values, it has certain defects. Helbing and Tilch[23] compiled a large amount of empirical data to overcome this shortcoming and proposed a generalized force (GF) model. The same as GHR model, GF model considered the effect of relative speed, too, but the model ignored the situation where the velocity of the follower is equal to or less than the velocity of the leader. Then, Jiang *et al.*[24] proposed the full velocity difference (FVD) model, which considers the positive relative velocity. Therefore, the FVD model can describe the actual traffic flow better compared to the OV and GF models during the car-following process. Its formula reads

$$\frac{\mathrm{d}v_n(t)}{\mathrm{d}t} = \alpha\left[V\left(\Delta x_n(t)\right) - v_n(t)\right] + \lambda \Delta v_n(t), \tag{4}$$

in which $V(\theta_n(t))$ represents the relative velocity and λ is its sensitivity coefficient. In 2019, Yan *et al.*[25] improved the FVD by taking the optimal velocity difference and the electronic throttle angle difference of the preceding vehicle into account so as to explain the current complex traffic situation.

In the model, driver's response is mainly coming from the stimulus of both speed difference and headway. However, since Michaels[26] introduced psychology-related theories into the car-following model for the first time, a series of follow-up studies (e.g., Winsum[27]) showed that psychological characteristics are indeed related to the stability of traffic flow. Its main performance is that visual angle can be used to replace headway together with angular velocity, which can be used to replace speed difference in some engineering car-following models. Therefore, Andersen and Sauer[28] proposed the driving by visual angle (DVA) model by taking visual angle into account based on Helly's[19] model.

Combined the FVD with DVA model, Jin *et al.*[29] developed the visual angle model (VAM) which takes both positive velocity difference and visual angle into account defined as

$$\frac{\mathrm{d}v_n(t)}{\mathrm{d}t} = \alpha\left[V\left(\theta_n(t)\right) - v_n(t)\right] - \lambda \frac{\mathrm{d}}{\mathrm{d}t}\theta_n(t), \tag{5}$$

where $V(\theta_n(t))$ represents the optimal velocity according to the visual angle of the driver, and $\theta_n(t)$ represents visual angle observed by the driver of car n at time t, as shown in Fig. 1.

As we all know, car-following behavior is a human-related process, and inserting visual angle into the FVD can access to 3D parameters information directly, which is closer to reality. However, in order to reduce gasoline consumption and stop-and-go while driving, many drivers always try to keep the vehicle as smooth as possible, which means that drivers

will control the headway far enough to accelerate, but in order to avoid the repeated deceleration, the driver may drive smoothly at the original speed rather than accelerating. Therefore, in addition to the influence of visual angle and relative speed, driver's stabilizing driving behavior can also affect the driving behavior, and for this reason, based on the VAM, in this paper we propose an improved car-following model by taking the effect of visual angle, anticipated time and driver's stabilizing driving behavior into account.

Bifurcation is defined as the process in which the nonlinear dynamic parameters of the system continuously change and reach a certain critical point, which causes the global nature of the system to change. In 1978, Huilgol[30] firstly introduced the bifurcation theory to the nonlinear dynamics of vehicle systems, which aroused the enthusiasm of traffic scholars around the world to study the stability of vehicle systems. With the continuous development of bifurcation analysis theory, Igarashi *et al.*[31] and Orosz *et al.*[32] selected different optimal velocity functions to study the bifurcation phenomenon in the OV model, and obtained the similar conclusions, which was later extended to the OVM with a single fixed delay by Yamamoto *et al.*[33] performed Hopf bifurcation analysis for the dissipative system with asymmetric interaction including the OVM. It is generally found that a bifurcation structure is related to the multiple traffic jams via the transitions of emerging clusters (i.e., traveling waves). In order to further explore the relationship between traffic state and bifurcation, in 2004, Gasser *et al.*[34] conducted a series of car-following models with bifurcation analyses. They found that the instability of the neutral stable solution increased in optimal velocity models is normally owing to the happen of the Hopf bifurcation. Jin *et al.*[35] conducted a bifurcation analysis for the FVD model to study the effect of bifurcation behavior on traffic congestion and stability of the system. More recently, Zhang *et al.*[36] studied the traditional velocity difference model considering time delays. They found that bifurcation happened corresponding to the emergence of traffic congestion in continuous traffic flow. Nowadays, a great progress on traffic flow has been made. However, it is still essential to explore and grasp the nonlinear characteristic of traffic information so as to eliminate the traffic jams.

Through the review of the development of traffic flow theory, we can find that few studies have comprehensively considered the driver's visual angle, anticipated time and driver's stable driving behavior to explore the impact of these characteristics on car-following behavior. While the article focuses on three human factors, comprehensively considers the driver's visual angle, anticipated time and stable driving behavior to explore the impact of driver behavior factors on car-following behavior. Then the influence of various factors on the stability of traffic flow is obtained through the linear, nonlinear analysis and numerical simulation. Finally, the rationality of the improved model is verified by parameter calibration.

The specific contribution of this paper are as follows:

(1) Providing theoretical support for the establishment of intelligent transportation systems. In the process of developing self-driving vehicles, robots can be used to simulate human driving, and the optimal human psycho-physiological characteristics are set during the robot programming, so as to achieve the maximum safety and optimal efficiency of the traffic flow.

(2) Providing references for traffic management systems. In terms of traffic safety, the optimal driver's psychological-physical characteristics obtained from the study can be used as the reference standard to strictly review the driver's driving qualification.

The following is the framework of the article. First of all, we make an overview of the development of the traffic flow in Section 1. Then we take visual angle, anticipated time and stabilizing driving behavior into account and put forward a new visual angle model in Section 2. In Section 3, the neutral stability curve is carried out through linear stability analysis. In Section 4 we conduct bifurcation analysis for the improved model and study the influence of the three driver's behavior on Hopf bifurcation. Through the numerical calculation, the time-dependent Ginzburg–Landau (TDGL) equation and the modified Korteweg–de Vries (mKdV) equation are given respectively in Sections 5 and 6. Then in Section 7, parameter calibration and numerical simulations are carried out and numerical results are discussed. Finally, we obtain the conclusions in Section 8.

2. The extended car-following model

All of the previous car-following models are developed based on the ideal state that the driver's immediate response to traffic conditions is absolutely rational, meanwhile, drivers have a great ability to perceive the traffic information, such as headway, velocity and acceleration. However, there are few psychological studies can prove this. Although some basic factors affecting the driving behavior, such as time delays, inaccuracies, and anticipated time have been taken into account in the car-following model, the headway and the relative velocity always play the most direct role in driver's perception. The improved model in this paper is proposed based on the theory, considering from a psychological perspective, that numerous of studies have showed that psychological effects can affect driving behavior, and the results of these studies can be applied to car-following models. The most essential research results are that visual information is strongly related to the driver's driving.

Considering both the physical and psychological characteristics of follower, we insert a visual angle of follower's driver into the car-following model rather than the headway and the difference of speed, whose relationship is displayed in

Fig. 1,

$$\theta_n(t) = \frac{w_{n-1}}{\Delta x_n(t) - l_{n-1}}, \tag{6}$$

where $\theta_n(t)$ is defined as the visual angle which is measured by the driver of the nth car at time t, $\Delta x_n(t) = x_{n+1}(t) - x_n(t)$ is the headway between the preceding $(n+1)$th car and the following nth car, and l_{n-1} and w_{n-1} represent the length and the width of the $(n-1)$th car, respectively.

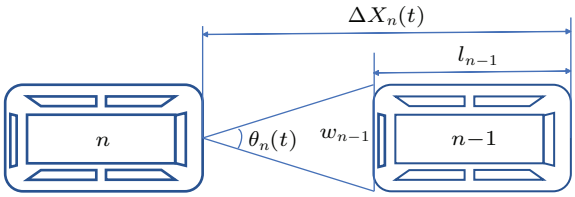


Fig. 1. Car-following model considering the visual angle.

In view of the above knowledge, we developed an improved car-following model considering the visual angle and anticipated time with stabilizing driving behavior. The dynamical equation is proposed as follows:

$$\begin{aligned}\frac{\mathrm{d}v_n(t)}{\mathrm{d}t} &= \alpha\left[V(\theta_n(t)) - v_n(t)\right] + \varepsilon\frac{w_{n-1}}{(h-l_{n-1})^2} \\ &\times \left(v_n(t+\tau) - v_n(t)\right) + \gamma V'(\theta_0)\left(h - \Delta x_n(t)\right),\end{aligned} \tag{7}$$

where α is known as the sensitivity coefficient of drivers to the difference between the current speed and desired speed. $v_n(t)$ denotes the speed of car n at time t, ε and γ are defined as the sensitivity parameter of time-delayed velocity difference and steady-state control effects respectively, and τ is the anticipated time. Furthermore, V represents the optimal velocity whose mathematical expression is defined as follows:

$$V(x) = v^e\frac{x^2}{1+x^2}, \tag{8}$$

where $v^e = \max V(x) > 0$ is called the desired speed.

Equation (7) proved that the visual angle stimulus can really affect the response of driver to follower. Since car-following behavior is closely related to human decision-making and response, it needs to take human's limits on judging headway and velocity stimulus into account. Therefore, considering driver's visual angle factor can fit to the real traffic flow better.

3. Linear stability analysis

In this section, we conduct the prerequisites for the stability of the improved model by linear analysis. For a uniform traffic flow, all vehicles have the same characteristics, including everyone in the unified system is moving at the optimal velocity $V(\theta_0)$ and the same headway h, and the visual angle $\theta_n(t)$ remains the same. Obviously, we can obtain

$$x_n^0 = hn + V(\theta_0)t, \quad h = L/N, \tag{9}$$

where $V(\theta_0)$ represents the optimal velocity in the uniform traffic flow, $\theta_0 = w_{n-1}/\left(h - l_{n-1}\right)$ represents the visual angle of follower when driver drives with a stable headway, and N and L denotes the number of total vehicle and the length of road respectively. Giving a small perturbation $y_n(t)$, we can obtain

$$x_n = hn + V(\theta_0)t + y_n(t). \tag{10}$$

By linearizing the equation as follows:

$$\begin{aligned}\frac{\mathrm{d}y_n^2(t)}{\mathrm{d}t^2} &= \alpha\left[-V'(\theta_0)\frac{w_{n-1}}{\left(h-l_{n-1}\right)^2}\Delta y_n(t) - y_n'(t)\right] \\ &+ \varepsilon\frac{w_{n-1}}{\left(h-l_{n-1}\right)^2}y_n''(t)\cdot\tau - \gamma V'(\theta_0)\Delta y_n(t),\end{aligned} \tag{11}$$

where $V'(\theta_0) = \mathrm{d}V(\theta)/\mathrm{d}\theta|_{\theta=\theta_0}$, and expanding $y_n(t)$ with the form of $y_n(t) = \mathrm{e}^{\mathrm{i}kn+zt}$, it follows

$$\begin{aligned}z^2 &= \alpha\left[-V'(\theta_0)\frac{w_{n-1}}{\left(h-l_{n-1}\right)^2}\left(\mathrm{e}^{\mathrm{i}k}-1\right) - z\right] \\ &+ \varepsilon\frac{w_{n-1}}{\left(h-l_{n-1}\right)^2}z^2\cdot\tau - \gamma V'(\theta_0)\left(\mathrm{e}^{\mathrm{i}k}-1\right).\end{aligned} \tag{12}$$

Expanding $z = z_1(\mathrm{i}k) + z_2(\mathrm{i}k)^2 + \cdots$, and substituting it into Eq. (12), we can gain the first-order and second-order terms of coefficients in the expression of z as follows:

$$\begin{aligned}z_1 &= -\frac{\left(\alpha\frac{w_{n-1}}{\left(h-l_{n-1}\right)^2} + \gamma\right)V'(\theta_0)}{\alpha}, \\ \alpha z_2 &= \left(\varepsilon\frac{w_{n-1}}{\left(h-l_{n-1}\right)^2}\tau - 1\right)z_1^2 \\ &- \frac{\alpha}{2}\frac{w_{n-1}}{\left(h-l_{n-1}\right)^2}V'(\theta_0) - \frac{\gamma}{2}V'(\theta_0).\end{aligned} \tag{13}$$

Integrating the two formulas, we can obtain the neutral stability conditions

$$\alpha = 2\left(\varepsilon\frac{w_{n-1}}{\left(h-l_{n-1}\right)^2}\tau - 1\right)\left(\frac{w_{n-1}}{\left(h-l_{n-1}\right)^2} + \frac{\gamma}{\alpha}\right)V'(\theta_0). \tag{14}$$

With small disturbances, the neutral stability condition of the uniform traffic flow is as follows:

$$\alpha > 2\left(\varepsilon\frac{w_{n-1}}{\left(h-l_{n-1}\right)^2}\tau - 1\right)\left(\frac{w_{n-1}}{\left(h-l_{n-1}\right)^2} + \frac{\gamma}{\alpha}\right)V'(\theta_0). \tag{15}$$

When α is satisfied with the condition, the traffic is stable with small disturbances. Otherwise, the traffic will become unstable.

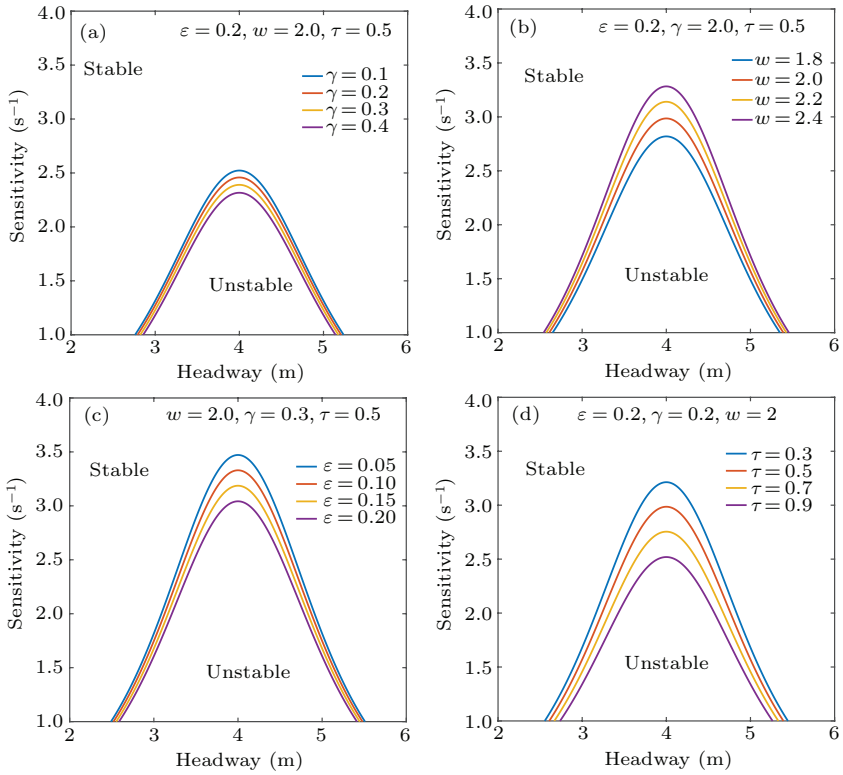


Fig. 2. Neutral stability curve with different γ, w, ε and τ.

Figure 2 depicts the neutral stability curve which describes the functional relationship between the headway and sensitivity coefficient space. As we can see, every neutral stability curve has a critical point (h_c, α_c) with different γ, w, ε and τ, respectively. The stability graph is separated into two parts by the critical curve, among which, one represents stability region, and the other represents instability region. Each point on the line represents a critical point for the stability to instability region. When $\alpha > \alpha_c$, regardless of the headway, traffic flow will always remain stable, otherwise congestion may occur. In other words, the traffic flow will keep going above the neutral stability curve and congestion is impossible to happen. While under the curve, the traffic flow density increased along with the increased possibility of congestion. As shown in Figs. 2(a), 2(c) and 2(d), when fixing other parameters at a proper value, the vertices of the curve gradually decrease with the increases of γ, ε and τ respectively. However, they play different roles for traffic flow stability. Instead, Fig. 2(b) describes the instability regions increase with the increasing of w gradually when fixing $\varepsilon = 0.2\ \mathrm{s}^{-1}$, $\gamma = 0.2\ \mathrm{m}^{-1}$ and $\tau = 0.5$ s. From this, we conclude that γ, ε and τ have a positive effect in the traffic stability, which is opposite to w.

4. Bifurcation analysis and simulation

In this section, we use the theoretical analysis to explore the bifurcation behavior of the new model first of all so as to study the correspondence between the critical point of Hopf bifurcation and instability, and then conduct the numerical simulation to display the impact of various parameters on the bifurcation behavior intuitively. Equation (7) can be rewritten as

$$\begin{aligned}\frac{\mathrm{d}x_n(t)}{\mathrm{d}t} &= v_n(t)\\ \frac{\mathrm{d}v_n(t)}{\mathrm{d}t} &= \alpha\left[V(\theta_n(t)) - v_n(t)\right] + \varepsilon\frac{w_{n-1}}{(h-l_{n-1})^2}\\ &\quad\times\left(v_n(t+\tau) - v_n(t)\right)\\ &\quad+\gamma V'(\theta_0)\left(h - \Delta x_n(t)\right).\end{aligned} \tag{16}$$

The uniform traffic state is denoted as such a state that vehicles have a constant headway x and optimal velocity $V(x)$. Suppose $\xi_n(t)$ and $\eta_n(t)$ be a small deviation to the steady state, while $x_n(t) = x_n^0(t) + \xi_n(t)$, $v_n(t) = V(\theta_0) + \eta_n(t)$, and linearize the equation as follows:

$$\begin{aligned}\frac{\mathrm{d}\xi_n(t)}{\mathrm{d}t} &= \eta_n(t),\\ \frac{\mathrm{d}\eta_n(t)}{\mathrm{d}t} &= \alpha\left[-V'(\theta_0)\frac{w_{n-1}}{(h-l_{n-1})^2}(\xi_{n+1} - \xi_n) - \eta_n\right]\\ &\quad+\varepsilon\frac{w_{n-1}}{(h-l_{n-1})^2}\eta_n'(t)\cdot\tau\\ &\quad-\gamma V'(\theta_0)(\xi_{n+1} - \xi_n).\end{aligned} \tag{17}$$

Through analyzing Eq. (17), we obtain the linearized equation as follows:

$$\begin{pmatrix}\frac{\mathrm{d}\xi_n}{\mathrm{d}t}\\ \frac{\mathrm{d}\eta_n}{\mathrm{d}t}\end{pmatrix} = \begin{pmatrix}O & E\\ A & B\end{pmatrix}\begin{pmatrix}\xi_n\\ \eta_n\end{pmatrix} = H\begin{pmatrix}\xi_n\\ \eta_n\end{pmatrix}, \tag{18}$$

where $\xi_n = (\xi_1, \xi_2, \xi_3, \ldots, \xi_n)^{\mathrm{T}}$, $\eta_n = (\eta_1, \eta_2, \eta_3, \ldots, \eta_n)^{\mathrm{T}}$, O is the $N \times N$ null matrix, and E is the $N \times N$ identity matrix.

$$A = \begin{bmatrix} \frac{\left(\alpha \frac{w_{n-1}}{\left(h-l_{n-1}\right)^2}+\gamma\right)V'(\theta_0)}{1-\varepsilon \frac{w_{n-1}}{\left(h-l_{n-1}\right)^2}\cdot\tau} & -\frac{\left(\alpha \frac{w_{n-1}}{\left(h-l_{n-1}\right)^2}+\gamma\right)V'(\theta_0)}{1-\varepsilon \frac{w_{n-1}}{\left(h-l_{n-1}\right)^2}\cdot\tau} & 0 & \cdots & 0 \\ 0 & \ddots & \ddots & \ddots & \vdots \\ \vdots & \ddots & \ddots & \ddots & 0 \\ 0 & \cdots & \cdots & \ddots & -\frac{\left(\alpha \frac{w_{n-1}}{\left(h-l_{n-1}\right)^2}+\gamma\right)V'(\theta_0)}{1-\varepsilon \frac{w_{n-1}}{\left(h-l_{n-1}\right)^2}\cdot\tau} \\ -\frac{\left(\alpha \frac{w_{n-1}}{\left(h-l_{n-1}\right)^2}+\gamma\right)V'(\theta_0)}{1-\varepsilon \frac{w_{n-1}}{\left(h-l_{n-1}\right)^2}\cdot\tau} & 0 & \cdots & 0 & \frac{\left(\alpha \frac{w_{n-1}}{\left(h-l_{n-1}\right)^2}+\gamma\right)V'(\theta_0)}{1-\varepsilon \frac{w_{n-1}}{\left(h-l_{n-1}\right)^2}\cdot\tau} \end{bmatrix}_{N\times N}, \tag{19}$$

$$B = \begin{bmatrix} -\frac{\alpha}{1-\varepsilon \frac{w_{n-1}}{\left(h-l_{n-1}\right)^2}\cdot\tau} & 0 & \cdots & 0 \\ 0 & \cdots & \cdots & \vdots \\ \vdots & \cdots & \cdots & \vdots \\ \vdots & \cdots & \cdots & 0 \\ 0 & \cdots & 0 & -\frac{\alpha}{1-\varepsilon \frac{w_{n-1}}{\left(h-l_{n-1}\right)^2}\cdot\tau} \end{bmatrix}_{N\times N}. \tag{20}$$

Suppose $\beta = \left(\alpha \frac{w_{n-1}}{\left(h-l_{n-1}\right)^2}+\gamma\right)V'(\theta_0)$. When N is odd number, the corresponding characteristic equation of H is obtained from Eq. (18),

$$\begin{aligned} &\det\left(\lambda^2 - \lambda B - A\right) \\ &= \left(\lambda^2 + \lambda \frac{\alpha}{1-\varepsilon \frac{w_{n-1}}{\left(h-l_{n-1}\right)^2}\cdot\tau} - \frac{\beta}{1-\varepsilon \frac{w_{n-1}}{\left(h-l_{n-1}\right)^2}\cdot\tau}\right)^N \\ &\quad + \left(\frac{\beta}{1-\varepsilon \frac{w_{n-1}}{\left(h-l_{n-1}\right)^2}\cdot\tau}\right)^N = 0. \end{aligned} \tag{21}$$

Use the Hopf theorem to find the Hopf bifurcation point L^*. It can be found that when a smooth family of eigenvalues $\lambda = \psi \pm \mathrm{i}\omega$ appears, the Hopf bifurcation condition is satisfied, and the bifurcation occurs.

Substituting $\lambda = \psi \pm \mathrm{i}\omega$ into Eq. (19), one obtains

$$\begin{aligned} &\psi^2 + \mathrm{i}2\psi\omega - \omega^2 + \frac{\alpha}{1-\varepsilon \frac{w_{n-1}}{\left(h-l_{n-1}\right)^2}\cdot\tau}\psi \\ &\quad + \mathrm{i}\frac{\alpha}{1-\varepsilon \frac{w_{n-1}}{\left(h-l_{n-1}\right)^2}\cdot\tau}\omega - \frac{\beta}{1-\varepsilon \frac{w_{n-1}}{\left(h-l_{n-1}\right)^2}\cdot\tau} \\ &= -\left(\frac{\beta}{1-\varepsilon \frac{w_{n-1}}{\left(h-l_{n-1}\right)^2}\cdot\tau}\right)\left(\cos\frac{2k\pi}{N} + \mathrm{i}\sin\frac{2k\pi}{N}\right), \end{aligned} \tag{22}$$

where $k \in \{1, 2, \ldots, N\}$.

Separating the real and imaginary parts of Eq. (22), the result shows

$$\begin{aligned} &-\omega^2\left(1-\varepsilon \frac{w_{n-1}}{\left(h-l_{n-1}\right)^2}\cdot\tau\right) + \psi\alpha \\ &= -\beta\left(\cos\frac{2k\pi}{N} - 1\right), \\ &2\psi\omega\left(1-\varepsilon \frac{w_{n-1}}{\left(h-l_{n-1}\right)^2}\cdot\tau\right) + \omega\alpha \\ &= -\beta\sin\frac{2k\pi}{N}. \end{aligned} \tag{23}$$

Obviously, the whole set of eigenvalues is centered on $\left(-1/2,\ 0\right)$ as a symmetry point. For $k = N$, the points $(\psi, \omega) = (0, 0)$ and $(\psi, \omega) = \left(\frac{-\alpha}{1-\varepsilon \frac{w_{n-1}}{\left(h-l_{n-1}\right)^2}\cdot\tau},\ 0\right)$ are the solutions of the system for every β, γ, τ and ε. As for every stationary k and $k \neq N$, the distribution of eigenvalues of Eq. (23) with regard to the parameter $\beta > 0$ is shown in Fig. 3. The eigenvalues are located at the point $P = (0, 0)$ and $Q = (-1, 0)$, respectively, for $\beta = 0$, $\varepsilon = 0$ and $\alpha = 1\ \mathrm{s}^{-1}$. However, when the parameter β increases, two eigenvalues associated with $k = N$ stay in $(0, 0)$ and $\left(\frac{-\alpha\left(h-l_{n-1}\right)^2}{\left(h-l_{n-1}\right)^2-\varepsilon w_{n-1}\cdot\tau},\ 0\right)$, respectively, and all the eigenvalues separate from each other flowing along the hyperbolic branches except for the two eigenvalues stay in points P and Q respectively (for $k = N$). Regarding a sufficiently small parameter $\beta > 0$, we can see that all the eigenvalues stay in the left complex plane in Fig. 3, demonstrating that the traffic flow is gradually becoming stable. It is easy to comprehend because the optimal acceleration is a sufficiently small quantity for a sufficiently small quantity when parameter $\beta > 0$ is small enough, what means that every vehicle is moving with a constant velocity and headway on the road. With the increasing of β, a pair of complex conjugate eigenvalues might cross the imaginary y-axis and causing traffic flow to move to an unstable state.

When Hopf bifurcation happens, there are only a pair of imaginary roots $\lambda_{1,2} = \pm\mathrm{i}\omega$. In Fig. 3, all of other $(N-2)$ eigenvalues are located in the left complex plane when a pair of pure imaginary roots appears at the first time (for $k = 1$ and

$k = N-1$).

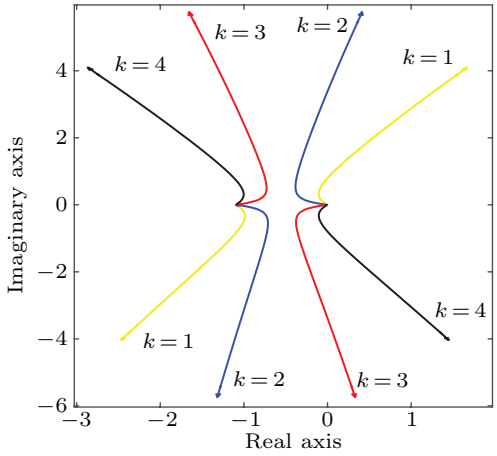


Fig. 3. Eigenvalues of the system for $N = 5$, $\alpha = 1\ \mathrm{s}^{-1}$, $\varepsilon = 0.05\ \mathrm{s}^{-1}$, and $\tau = 0.4$ s.

Inserting $\lambda = \mathrm{i}\omega$, $\psi = 0$ and $k = 1$ into Eq. (23), we can obtain

$$-\omega^2\left(1-\lambda\frac{w_{n-1}}{(h-l_{n-1})^2}\cdot\tau\right) = -\beta\left(\cos\frac{2\pi}{N}-1\right),$$
$$\omega\alpha = -\beta\sin\frac{2\pi}{N}. \tag{24}$$

The critical condition is as follows:

$$\begin{aligned}\beta &= \frac{\alpha^2}{1+\cos\frac{2\pi}{N}}\frac{1}{\varepsilon\frac{w_{n-1}}{(h-l_{n-1})^2}\tau-1}\\ &> \frac{\alpha^2}{2}\frac{1}{\varepsilon\frac{w_{n-1}}{(h-l_{n-1})^2}\tau-1}.\end{aligned} \tag{25}$$

Define the parameter β that satisfies the critical relation as β_1. When $\varepsilon = 0$ and $\gamma = 0$, Eq. (25) is just coincided with the result of the OV model obtained in Ref. [47], and the equation can be re-expressed as follows:

$$\begin{aligned}V'(\theta_0) &= \frac{\alpha^2}{1+\cos\frac{2\pi}{N}}\frac{1}{\varepsilon\frac{w_{n-1}}{(h-l_{n-1})^2}\tau-1}\frac{1}{\alpha\frac{w_{n-1}}{(h-l_{n-1})^2}+\gamma}\\ &> \frac{\alpha^2}{2}\frac{1}{\varepsilon\frac{w_{n-1}}{(h-l_{n-1})^2}\tau-1}\frac{1}{\alpha\frac{w_{n-1}}{(h-l_{n-1})^2}+\gamma},\end{aligned} \tag{26}$$

which is just contrary to the result shown in Eq. (15).

Next, differentiation of the characteristic Eq. (27) brings about the essential condition for the Hopf bifurcation, i.e.,

$$\psi'(\beta) = \frac{-\sin^2\frac{2k\pi}{N}}{\alpha\left(\cos\frac{2k\pi}{N}+1\right)} < 0. \tag{27}$$

Obviously, from Eq. (27), the Hopf condition $\psi(\beta_1) < 0$ is satisfied absolutely. Therefore, the Hopf bifurcation occurs in our system. We can obtain the critical length L^* from the following equation:

$$V'\left(\frac{w_{n-1}}{\frac{L^*}{N}-l_{n-1}}\right) = \frac{\alpha^2}{1+\cos\frac{2\pi}{N}}\frac{1}{\varepsilon\frac{w_{n-1}}{(h-l_{n-1})^2}\tau-1}$$
$$\times\frac{1}{\alpha\frac{w_{n-1}}{(h-l_{n-1})^2}+\gamma}. \tag{28}$$

The spatial variation of Hopf's relation (28) is displayed in the three-dimensional diagram of Fig. 4. The yellow surface is graph of

$$V'\left(\frac{w_{n-1}}{\frac{L}{N}-l_{n-1}}\right) = \frac{2\frac{L}{N}}{\left(1+\left(\frac{L}{N}\right)^2\right)^2},$$

while the blue surface is the spatial variation curve of

$$V'\left(\frac{w_{n-1}}{\frac{L^*}{N}-l_{n-1}}\right) = \frac{\alpha^2}{1+\cos\frac{2\pi}{N}}\frac{1}{\varepsilon\frac{w_{n-1}}{(h-l_{n-1})^2}\tau-1}$$
$$\times\frac{1}{\alpha\frac{w_{n-1}}{(h-l_{n-1})^2}+\gamma}.$$

The intersection of these two surfaces corresponds to the critical point when Hopf bifurcation occurs.

In order to display and compare the effect of τ, ε and γ on Hopf bifurcation more intuitively, Fig. 5 shows the two-dimensional (L,N)-plane corresponding to Fig. 4, respectively, which reveals the instability regions of the system, and in which the first pair of eigenvalues have positive real parts drawn in yellow. The Hopf curve consists of the set of all intersections (L,N) of the first pair of eigenvalues and the second pair of eigenvalues, that is, the boundary between the blue plane and the yellow plane in Fig. 4. It is uncovered that the sensitivity anticipated time τ, ε and γ play a different role on the occurrence of Hopf bifurcation. Figures 5(a) and 5(b) indicate the critical point (L_C, N_C) of Hopf bifurcation from $(4.1, 3.8)$ to $(5.1, 8.9)$ because of the increasing of anticipated time τ from 1 to 2 and fixing the sensitivity coefficient $\varepsilon = 0.05\ \mathrm{s}^{-1}$ and $\gamma = 0.8\ \mathrm{m}^{-1}$. In Figs. 5(c) and (d), the critical point (L_C, N_C) of Hopf bifurcation changes from $(4.1, 3.8)$ to $(5.4, 10.8)$ with the increasing of ε while keeping anticipated time τ and γ unchanged. It displays the instability area decreases because of the increasing of ε. In Figs. 5(e) and 5(f), the critical point (L_C, N_C) of Hopf bifurcation changes from $(5.8, 11.6)$ to $(3.9, 1.8)$ with the decrease of the sensitivity γ and fixing the anticipated time $\tau = 0.4$ s and $\varepsilon = 0.05\ \mathrm{s}^{-1}$. It shows the instability area increases with the decrease of γ from $0.8\ \mathrm{m}^{-1}$ to $0.65\ \mathrm{m}^{-1}$. Therefore, parameter τ, ε and γ all can inhibit the occurrence of bifurcation, it means they all contribute to the system's stability despite the different effect in the critical point region of Hopf bifurcation.

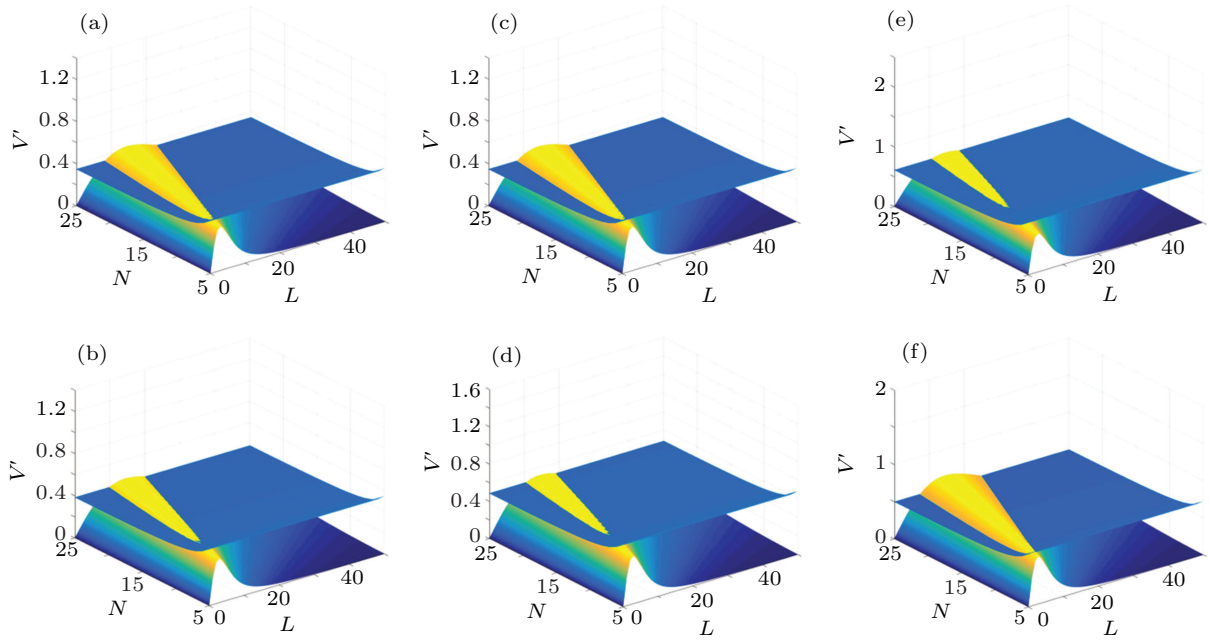


Fig. 4. Side view for $\alpha = 1\ \mathrm{s}^{-1}$, $v^e = 1$ m/s with different values γ, ε and τ: (a) $\tau = 1$ s, $\varepsilon = 0.05\ \mathrm{s}^{-1}$, $\gamma = 0.8\ \mathrm{m}^{-1}$; (b) $\tau = 2$ s, $\varepsilon = 0.05\ \mathrm{s}^{-1}$, $\gamma = 0.8\ \mathrm{m}^{-1}$; (c) $\tau = 1$ s, $\varepsilon = 0.05\ \mathrm{s}^{-1}$, $\gamma = 0.8\ \mathrm{m}^{-1}$; (d) $\tau = 1$ s, $\varepsilon = 0.1\ \mathrm{s}^{-1}$, $\gamma = 0.8\ \mathrm{m}^{-1}$; (e) $\tau = 0.4$ s, $\varepsilon = 0.05\ \mathrm{s}^{-1}$, $\gamma = 0.8\ \mathrm{m}^{-1}$; (f) $\tau = 0.4$ s, $\varepsilon = 0.05\ \mathrm{s}^{-1}$, $\gamma = 0.65\ \mathrm{m}^{-1}$.

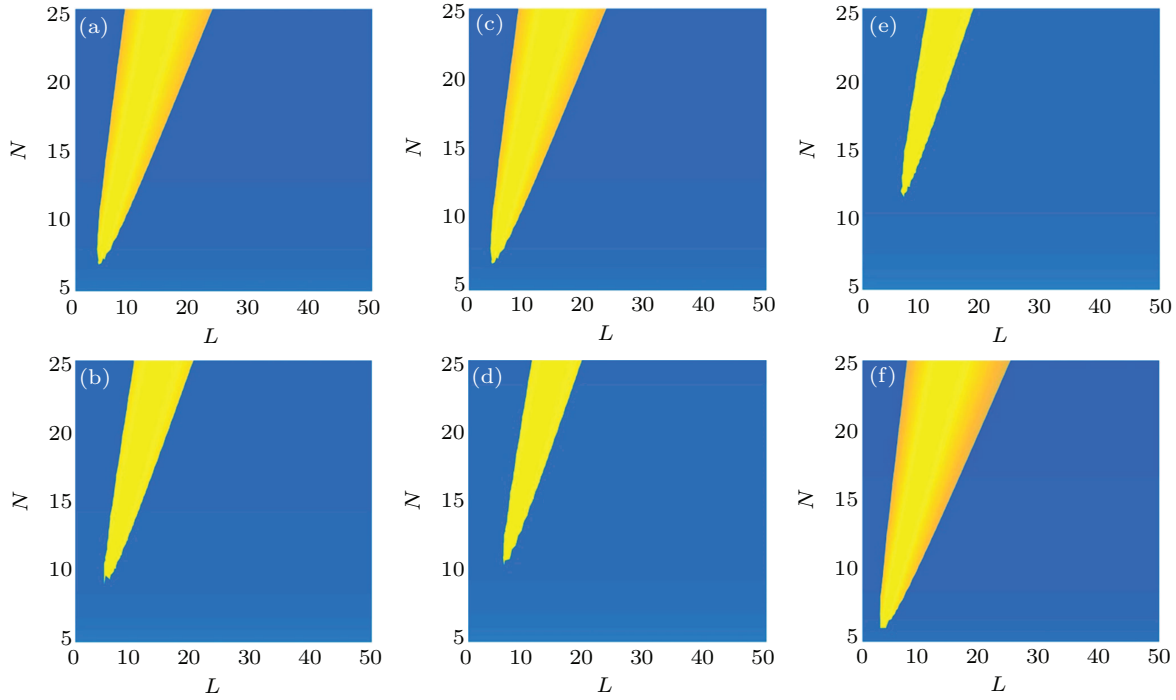


Fig. 5. Side view for $\alpha = 1\ \mathrm{s}^{-1}$, $v^e = 1$ m/s with different values γ, ε and τ: (a) $\tau = 1$ s, $\varepsilon = 0.05\ \mathrm{s}^{-1}$, $\gamma = 0.8\ \mathrm{m}^{-1}$; (b) $\tau = 2$ s, $\varepsilon = 0.05\ \mathrm{s}^{-1}$, $\gamma = 0.8\ \mathrm{m}^{-1}$; (c) $\tau = 1$ s, $\varepsilon = 0.05\ \mathrm{s}^{-1}$, $\gamma = 0.8\ \mathrm{m}^{-1}$; (d) $\tau = 1$ s, $\varepsilon = 0.1\ \mathrm{s}^{-1}$, $\gamma = 0.8\ \mathrm{m}^{-1}$; (e) $\tau = 0.4$ s, $\varepsilon = 0.05\ \mathrm{s}^{-1}$, $\gamma = 0.8\ \mathrm{m}^{-1}$; (f) $\tau = 0.4$ s, $\varepsilon = 0.05\ \mathrm{s}^{-1}$, $\gamma = 0.65\ \mathrm{m}^{-1}$.

5. The TDGL eqnarray

In this section, we carry out the nonlinear analysis of Eq. (7) so as to obtain the TDGL equation that fits the improved model traffic behavior best near the critical point (h_c, α_c). The slow scales for space variable n, time variable t and constant b are introduced, and the slow variables X and T are defined as follows:

$$X = \mu(n + bt), \quad T = \mu^3 t, \quad 0 < \mu \ll 1. \tag{29}$$

While $\Delta x_n(t)$ is defined as follows:

$$\Delta x_n(t) = h_c + \mu R(X, T), \tag{30}$$

where h_c stands for safety distance. By inserting Eqs. (29) and (30) to Eq. (31), along with the Taylor expanding to the fifth-order of μ, the nonlinear partial differential equation is shown as follows:

$$\mu^2 \left(-\alpha \frac{w_{n-1}}{(h - l_{n-1})^2} V' - \alpha b - \gamma V' \right) \partial_X R$$

$$+\mu^3\left(\frac{w_{n-1}}{(h-l_{n-1})^2}\left(\varepsilon\tau b^2-\frac{1}{2}aV'\right)-b^2-\gamma V'\right)\partial_X^2 R$$
$$+\mu^4\left(-\frac{1}{6}V'\right)\left(\alpha\frac{w_{n-1}}{(h-l_{n-1})^2}+\gamma\right)\partial_X^3 R-\alpha\mu^4\partial_T R$$
$$+\mu^5\left[2\left(\frac{w_{n-1}\cdot\varepsilon\tau b}{(h-l_{n-1})^2}-b\right)\partial_X\partial_T R\right.$$
$$\left.-\frac{1}{24}\left(\frac{w_{n-1}\cdot\alpha}{(h-l_{n-1})^2}V'+\gamma V'\right)\right]\partial_X^4 R=0. \tag{31}$$

We mainly consider the state where the traffic behavior is close to the critical point $\tau=\left(1+\mu^2\right)\tau_c$. By inserting $b=-\left(\frac{w_{n-1}}{(h-l_{n-1})^2}+\frac{\gamma}{\alpha}\right)V'$ into Eq. (31), the second-order and third-order terms of μ are eliminated from Eq. (31) and the equation is

$$\mu^4\partial_T R=\mu^3\left(\frac{w_{n-1}}{(h-l_{n-1})^2}\left(\frac{\varepsilon\tau b^2}{\alpha}-\frac{1}{2}V'\right)-\frac{b^2}{\alpha}-\frac{\gamma V'}{\alpha}\right)\partial_X^2 R$$
$$+\mu^4\left(-\frac{1}{6}V'\right)\left(\frac{w_{n-1}}{(h-l_{n-1})^2}+\frac{\gamma}{\alpha}\right)\partial_X^3 R$$
$$+\mu^5\left[\frac{2b}{\alpha}\left(\frac{w_{n-1}\cdot\varepsilon\tau}{(h-l_{n-1})^2}-1\right)\partial_X\partial_T R\right.$$
$$\left.-\frac{1}{24}\left(\frac{w_{n-1}}{(h-l_{n-1})^2}V'+\frac{\gamma}{\alpha}V'\right)\right]\partial_X^4 R=0. \tag{32}$$

Defining variables X and T as variables $x=\mu^{-1}X$ and $t=\mu^{-3}T$, and taking $S(x,t)=\mu R(X,T)$, we can obtain

$$\partial_t R=\left(\frac{w_{n-1}}{(h-l_{n-1})^2}\left(\frac{\varepsilon\tau b^2}{\alpha}-\frac{1}{2}V'\right)-\frac{b^2}{\alpha}-\frac{\gamma V'}{\alpha}\right)\partial_x^2 R$$
$$-\frac{1}{6}V'\left(\frac{w_{n-1}}{(h-l_{n-1})^2}+\frac{\gamma}{\alpha}\right)\partial_x^3 R$$
$$+\frac{2b}{\alpha}\left(\frac{w_{n-1}\cdot\varepsilon\tau}{(h-l_{n-1})^2}-1\right)\partial_x\partial_t R$$
$$-\frac{1}{24}\left(\frac{w_{n-1}}{(h-l_{n-1})^2}V'+\frac{\gamma}{\alpha}V'\right)\partial_x^4 R. \tag{33}$$

By adding term

$$\left(\frac{w_{n-1}}{(h-l_{n-1})^2}\left(\frac{\varepsilon\tau b^2}{\alpha}-\frac{1}{2}V'\right)-\frac{b^2}{\alpha}-\frac{\gamma V'}{\alpha}\right)\partial_x^2 S$$

on both sides of Eq. (30) and conducting variable conversion $t=t_1$,

$$x_1=x-\left(\frac{w_{n-1}}{(h-l_{n-1})^2}\left(\frac{\mu\tau b^2}{\alpha}-\frac{1}{2}V'\right)-\frac{b^2}{\alpha}-\frac{\gamma V'}{\alpha}\right)\partial_x^2 S$$

for Eq. (30), we get

$$\partial_{t1}S=\left(\partial_{x1}+\left(\frac{1}{2}V'+\mu\tau b\right)\partial_{x1}^2\right)$$
$$\times\left\{\left(-\frac{w_{n-1}}{(h-l_{n-1})^2}\left(\frac{1}{6}V'+\frac{\mu\tau b}{2}\right)+\frac{\gamma\tau}{2\mu}\right)\partial_{x1}^2 S\right.$$
$$\times\left(\left(-\frac{w_{n-1}}{(h-l_{n-1})^2}\left(\frac{1}{2}V'+\mu\tau\right)+\tau\left(\frac{\gamma}{\mu}-1\right)\right)S\right)$$
$$\left.+\frac{w_{n-1}}{(h-l_{n-1})^2}\frac{1}{2}V'''S^3\right\}. \tag{34}$$

By defining the thermodynamic potentials as follows:

$$\varphi(s)=-\left(-\frac{w_{n-1}}{(h-l_{n-1})^2}\right)\left(-\frac{w_{n-1}}{(h-l_{n-1})^2}\left(\frac{1}{2}V'+\mu\tau b\right)\right.$$
$$\left.+b\mu\tau\left(\frac{\gamma}{q}-1\right)\right)S^2-\frac{1}{24}V'''S^4 \tag{35}$$

and substitute Eq. (35) into Eq. (34), the TDGL equation is transformed as

$$\partial_{t1}S=-\left(\partial_{X1}+\left(\frac{1}{2}V'+\mu\tau b\right)\partial_{X1}^2\right)\frac{\partial\Phi(S)}{\partial S}, \tag{36}$$
$$\Phi(S)=\int d_{x1}\left[\frac{1}{2}\left(-\frac{w_{n-1}}{(h-l_{n-1})^2}\left(\frac{1}{6}V'+\frac{\mu\tau b}{2}\right)+\frac{b\gamma\tau}{2\mu}\right)(\mathrm{d}x_1 S)^2+\phi(S)\right], \tag{37}$$

where $\partial\Phi(S)/\partial S$ represents the function derivative. In addition to the simplest solution $S=0$, another two stable solutions have also been shown, one of which is a uniform solution

$$S(x_1,t_1)=\pm\left(\frac{\frac{3}{4}\left(-\frac{(h-l_{n-1})^2}{w_{n-1}}\right)\left(-\frac{w_{n-1}}{(h-l_{n-1})^2}\left(\frac{1}{2}V'+\mu\tau b\right)+b\mu\tau\left(\frac{\gamma}{\mu}-1\right)\right)}{V'''}\right)^{1/2} \tag{38}$$

and the other is the kink solution

$$S(x_1,t_1)=\pm\left(\frac{\frac{3}{4}\left(-\frac{(h-l_{n-1})^2}{w_{n-1}}\right)\left(-\frac{w_{n-1}}{(h-l_{n-1})}\left(\frac{1}{2}V'+\mu\tau b\right)+b\mu\tau\left(\frac{\gamma}{\mu}-1\right)\right)}{V'''}\right)^{1/2}$$

$$\times \tanh\left\{\left[\left(\frac{w_{n-1}}{(h-l_{n-1})}\left(\frac{1}{24}V'-\frac{\mu\tau b}{6}\right)+\frac{b\lambda\tau}{3\mu}\right)\left(-\frac{w_{n-1}}{(h-l_{n-1})}\left(\frac{1}{2}V'+\mu\tau b\right)\right)\times(x_1-x_0)\right]^{1/2}\right\}, \tag{39}$$

where x_0 is constant. Through analyzing Eq. (39), we can obtain a coexistence curve when following formula relations are met:

$$\partial\phi/\partial S=0,\quad \partial^2\phi/\partial S^2>0. \tag{40}$$

Inserting Eq. (35) into Eq. (40), we can obtain the coexistence curve with the original parameters

$$(\Delta s)_{\rm co}=s_{\rm c}\pm\left(\frac{\frac{3}{4}\left(-\frac{(h-l_{n-1})^2}{w_{n-1}}\right)\left(-\frac{w_{n-1}}{(h-l_{n-1})^2}\left(\frac{1}{2}V'+\mu\tau b\right)+bp\tau\left(\frac{\gamma}{\mu}-1\right)\right)}{V'''}\right)^{1/2}. \tag{41}$$

The spinodal line is based on the following conditions:

$$\partial^2\phi/\partial S^2=0. \tag{42}$$

By inserting Eq. (35) into Eq. (42), the relationship of the spinodal line is as follows:

$$(\Delta s)_{sp}=s_{\rm c}\pm\left(\frac{\frac{1}{4}\left(-\frac{(h-l_{n-1})^2}{w_{n-1}}\right)\left(-\frac{w_{n-1}}{(h-l_{n-1})^2}\left(\frac{1}{2}V'+\mu\tau b\right)+b\tau\left(\frac{\gamma}{\mu}-1\right)\right)}{V'''}\right)^{1/2}. \tag{43}$$

Based on the condition $\partial\phi/\partial S=0$ and Eq. (43), we can calculate the critical point containing the original parameters

$$\begin{aligned}&(\Delta x)_{\rm co}=h_{\rm c},\\&\alpha=2\left(\mu\frac{w_{n-1}}{\left(h-l_{n-1}\right)^2}\tau-1\right)\left(\frac{w_{n-1}}{\left(h-l_{n-1}\right)^2}+\frac{\gamma}{\alpha}\right)V'(\theta_0).\end{aligned} \tag{44}$$

6. The mKdV equation

Analogously, from the derivation of the TDGL equation, we take the slowly varying behavior into account at long wavelengths near critical point $(h_{\rm c},\alpha_{\rm c})$. We introduce the slow variable of space n and time t into the derivation of the TDGL equation. Taking $\alpha_{\rm c}=\frac{2w_{n-1}\left(\mu-V'(\theta_0)\right)}{(h-l)^2_{n-1}}-\frac{2b\gamma}{\varepsilon}$ and $\alpha_{\rm c}=\left(1+\mu^2\right)\alpha$ into Eq. (7), eliminating the second-order and third-order terms of μ, we get

$$\begin{aligned}&\mu^4\left(\partial_T R-g_1\partial_x^3R-g_2\partial_xR^3\right)\\&-\mu^5\left(g_3\partial_x^2R+g_4\partial_x^4R+g_5\partial_x^2R^3\right)=0.\end{aligned} \tag{45}$$

All of g_i are shown in Table 1.

Table 1. The coefficients g_i.

g_1	g_2
$\left(-\frac{w_{n-1}}{(h-l_{n-1})^2}\left(\frac{1}{6}V'+\frac{\varepsilon\tau_{\rm c}b}{2}\right)+\frac{bp\gamma\tau_{\rm c}}{2\varepsilon}\right)$	$\left(-\frac{w_{n-1}}{(h-l_{n-1})^2}\right)\frac{1}{2}V'''$
g_3	g_5
$\left(-\frac{w_{n-1}}{(h-l_{n-1})^2}\left(\frac{1}{2}V'+\varepsilon\tau_{\rm c}b\right)+b\tau_{\rm c}\left(\frac{\gamma}{\varepsilon}-1\right)\right)$	$\left(-\frac{w_{n-1}}{(h-l_{n-1})^2}\right)\frac{3}{4}V'''$
g_4	
$\left(\frac{w_{n-1}\cdot\varepsilon}{(h-l_{n-1})^2}-2b+\frac{\gamma p}{\varepsilon}\right)\left(-\frac{w_{n-1}}{(h-l_{n-1})^2}\left(\frac{1}{6}V'+\frac{\varepsilon\tau_{\rm c}b}{2}\right)+\frac{bp\gamma\tau_{\rm c}}{2\varepsilon}\right)-\frac{3}{4}V'''\left(-\frac{w_{n-1}}{(h-l_{n-1})^2}\right)\left(-\frac{w_{n-1}}{(h-l_{n-1})^2}\left(\frac{1}{6}V'+\frac{\varepsilon\tau_{\rm c}b}{2}\right)+\frac{bp\gamma\tau_{\rm c}}{2\varepsilon}\right)$	

In the table

$$V'=\mathrm{d}V(\Delta x_n)/\mathrm{d}t\,|_{\Delta x_n=h_{\rm c}},$$

$$V'''=\mathrm{d}^3V(\Delta x_n)/\mathrm{d}t^3\,|_{\Delta x_n=h_{\rm c}}.$$

In order to export the regularized equation, we give the following definition:

$$T=\frac{1}{g_1}T',\quad R=\sqrt{\frac{g_1}{g_2}}R'. \tag{46}$$

So, the standard mKdV equation with $O(\mu)$ correction term is obtained as

$$\begin{aligned}\partial_{T'}R'\ =\ &\partial_x^3R'-\partial_xR'^3\\&-\mu\left[\frac{g_3}{g_1}\partial_x^2R'+\frac{g_4}{g_1}\partial_x^4R'+\frac{g_5}{g_2}\partial_x^2R'^3\right].\end{aligned} \tag{47}$$

By ignoring the $O(\mu)$, the mKdV equation can be obtained by replacing the required solution with a kink solution

$$R'_0(X,T')=\sqrt{c}\tanh\sqrt{\frac{c}{2}}\left(X-cT'\right). \tag{48}$$

Then, assuming that $R'(X,T') = R'_0(X,T') + \mu R'_1(X,T')$ and considering the $O(\mu)$ correction term, in order to obtain the propagation velocity c for the kink solution, it can be based on the solvability condition as

$$\left(R'_0, M\left[R'\right]\right) \equiv \int_{-\infty}^{+\infty} \mathrm{d}X' R'_0 M\left[R'\right] = 0, \tag{49}$$

where

$$M\left[R'_0\right] = \frac{g_3}{g_1}\partial_X^2 R' + \frac{g_4}{g_1}\partial_X^4 R' + \frac{g_5}{g_2}\partial_X^2 R'^3,$$

and the general velocity c obtained by calculation is as follows:

$$c = \frac{5g_2g_3}{2g_2g_4 - 3g_1g_5}. \tag{50}$$

Therefore, the general kink–antikink solution of the headway from the mKdV equation is obtained as

$$\begin{aligned}\Delta x_n(t) = {} & h_{\mathrm{c}} \pm \sqrt{\frac{g_1 c}{g_2}\left(\frac{\tau}{\tau_{\mathrm{c}}} - 1\right)} \times \tanh\sqrt{\frac{c}{2}\left(\frac{\tau}{\tau_{\mathrm{c}}} - 1\right)} \\ & \times \left[n + (1 - cg_1)\left(\frac{\tau}{\tau_{\mathrm{c}}} - 1\right)t\right],\end{aligned} \tag{51}$$

where $V''' < 0$, and τ represents the reciprocal of the driver's sensitivity coefficient.

7. Simulation

7.1. Parameter calibration

In this part, 558 groups datasets of the 59th vehicle in the NGSIM database including velocity, acceleration and other factors are used to calibrate the optimal parameters. Considering that the modified dataset includes vehicle data in a non-car-following state, and existing the lane-changing behavior, therefore we make the following restrictions on car-following behavior.

(1) Car-following behavior should occur in the same lane, in other words, the data bar of Lane_ID should be the same value.

(2) Except for the first car, the selected leading car and following car, namely, preceding and following are not 0.

(3) In order to ensure that the vehicle stays in the car-following state, the headway should not be too large. Otherwise, the behavior change of the previous car will hardly affect the behavior of the target car.

Filtering by the above conditions, we can obtain the car-following data about the 59th car. Following is a partial data display.

Table 2. Car-following partial data of the 59th car.

Vehicle_ID	v_length	v_width	v_V el	v_A cc	Lane-ID	Preceding	Following	Headway
59	15	7	5.07	5.07	1	52	66	45.86
59	15	7	5.9	5.9	1	52	66	46.01
59	15	7	6.34	6.34	1	52	66	45.97
59	15	7	7.34	7.34	1	52	66	45.79
59	15	7	8.75	8.75	1	52	66	45.55
59	15	7	5.89	5.89	1	52	66	45.25
59	15	7	4.79	4.79	1	52	66	44.77
59	15	7	–5.9	–5.9	1	52	66	44.16
59	15	7	–5.75	–5.75	1	52	66	43.5
59	15	7	–2.67	–2.67	1	52	66	42.84
59	15	7	3.24	3.24	1	52	66	42.38
59	15	7	5.22	5.22	1	52	66	42.09
59	15	7	5.48	5.48	1	52	66	41.91
59	15	7	–1.76	–1.76	1	52	66	41.96
59	15	7	7.39	7.39	1	52	60	53.7
59	15	7	12.27	12.27	1	52	60	54.19
59	15	7	10.05	10.05	1	52	60	54.53
59	15	7	–0.37	–0.37	1	52	60	54.76
59	15	7	–8.18	–8.18	1	52	60	54.96
59	15	7	–8.71	–8.71	1	52	60	55.03
59	15	7	–5.43	–5.43	1	52	60	55.03

According to the model in this article, we can determine the parameters to be calibrated in this article and the input variables of the car-following model, then using the least square method to perform nonlinear optimization of the calibration parameters. The specific objective function expression we adopt is proposed by Ossen *et al.*,[37] whose core idea is as follows:

$$PI = \frac{\sqrt{\sum_{j=1}^{N}\left(a_j^{\mathrm{real}} - a_j^{\mathrm{sim}}\right)^2}}{\sqrt{\sum_{j=1}^{N}\left(a_j^{\mathrm{real}}\right)^2} + \sqrt{\sum_{j=1}^{N}\left(a_j^{\mathrm{sim}}\right)^2}}, \tag{52}$$

where N is the data group number, j donates the serial number

of data, a_j^{real} and a_j^{sim} represent actual acceleration and simulated acceleration respectively. Meanwhile, as an evaluation index describing the fitness of the parameter calibration, the smaller the PI, the closer the measured value is to the simulated value, that is, the better the applicability of the fitting result.

Moreover, both models select parameter combinations optimized by genetic algorithm and within 5% of the error range as their analysis objects. Then normalize each parameter and systematically cluster the optimized processing results of each parameter, the comparison of each parameter distribution of the clustering results of the two methods in Table 3.

As we can see in Table 3 that considering the anticipated time and stabilizing driving behavior can decrease the influence of α with the same data, which means anticipated time and stabilizing driving behavior can eliminate or weaken the adverse effects of optimal velocity in unified traffic flow effectively. In addition, the smaller h and the increase of $v_{\max}$ indicate that the minimum safety headway requirement is smaller in the stable traffic flow, and the maximum velocity that each vehicle can reach in the traffic flow has increased, which means the extended VAM is easier to steady than the VAM.

Table 3. Calibrated parameters.

Parameter	Range	OVM	Controlled OVM
α (s^{-1})	[0,2]	0.5164	0.4823
h (m)	[8,40]	31.5834	27.0565
$v_{\max}$ ($m \cdot s^{-1}$)	[20,40]	29.4532	34.4623
ε (s^{-1})	[−1,1]	0	0.7746
τ (s)	[0,2]	0	0.7179
γ (m^{-1})	[−1,1]	0	0.3481
PI		0.6624	0.6237

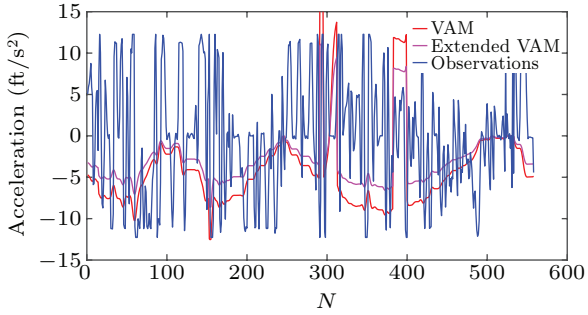


Fig. 6. Comparison of fitted values with observation data.

Figure 6 displays the fitness between the simulations and observations. It is not difficult to see that the red and pink curve maintain roughly the same trend with the blue line, where the pink and red lines denote the fitted value of extended VAM and VAM respectively, and the blue line represents the actual observation, indicating that the initial calibration coefficient set of the VAM and the extended VAM both can effectively predict the movement trend of the actual traffic flow during the acceleration, uniform velocity and deceleration phases. However, comparing the red and pink lines, obviously, the fitted value set of the extended VAM is closer to the observation in most data despite larger deviations in a few inflection points. And synthesizing the error value of all the data, it is found that the PI value is reduced from 0.6624 to 0.6237 after considering the gain and time-delay feedback control, which means that the controlled visual angle model can better reflect the complex actual flow.

7.2. Numerical simulation

In this section, numerical simulation of the improved model has been conducted so as to prove the obtained conclusions by using discrete equations. The discrete process is as follows:

$$
\begin{aligned}
&a\Delta t^2\left[V'\left[\theta_0\right]\left(\frac{-w_{n-1}}{\left(h-l_{n-1}\right)^2}\Delta x_{n+1}\left(t\right)\right)\right.\\
&\left.-V'\left[\theta_0\right]\left(\frac{-w_{n-1}}{\left(h-l_{n-1}\right)^2}\Delta x_n\left(t\right)\right)\right]-a\Delta t\cdot\frac{-w_{n-1}\cdot\varepsilon\tau}{\left(h-l_{n-1}\right)^2}\\
&+\varepsilon\Delta t\frac{w_{n-1}}{\left(h-l_{n-1}\right)^2}\left[\Delta x_n\left(t+\tau+\Delta t\right)-\Delta x_n\left(t+\tau\right)\right.\\
&\left.-\left(\Delta x_n\left(t+\Delta t\right)-\Delta x_n\left(t\right)\right)\right]\\
&-\gamma V'\left(\theta_0\right)\left[\Delta x_{n+1}\left(t+\Delta t\right)-\Delta x_{n+1}\left(t\right)\right]\\
&-\left[\Delta x_n\left(t+2\Delta t\right)-2\Delta x_n\left(t+\Delta t\right)+\Delta x_n\left(t\right)\right]=0. \qquad (53)
\end{aligned}
$$

The initial conditions are given as follows:

$$
\begin{cases}
\Delta x_j\left(0\right)=\Delta x_0=5.0, & x_j\left(1\right)=\Delta x_0=5.0, \quad j\neq 50,51;\\
\Delta x_j\left(1\right)=5.0-0.5, & j=50;\\
\Delta x_j\left(1\right)=5.0+0.5, & j=51.
\end{cases} \qquad (54)
$$

While $N=100$ veh and $\alpha=2\ s^{-1}$.

In Fig. 7, the improved car-following model carries out a series of simulations while controlling other parameters unchanged. The patterns in Figs. 7(a)–7(d) correspond to the variable w ($w=1.6,1.8,2.0,2.2$) respectively. Especially, when $w=1.6$ m, the traffic flow has the highest stability that means the car width of the front car has a certain influence on the follower's visual angle. As we can see that giving a small perturbation can induce initial stable traffic flow into an oscillating density wave. It can be clearly seen from the curvature change in Fig. 7 that the amplitude of the kink–antikink solution gradually increases with the increasing of parameter w. In other words, taking the vehicle width of the leader into account will interfere with the follower's perspective, which will inevitably affect the stability of the system and increase the possibility of congestion at the same time. The wider the vehicle's width, the more it can interfere with the driver's perspective, and the greater the possibility of the system's transition to instability region and traffic jams.

Figure 8 displays that the headway profiles and density waves for the preceding vehicle width w at $t=6000$ s corresponding to panels in Fig. 7 respectively. Obviously, as the

width of the vehicle increases, the amplitude of the headway gradually increases, which means considering the width of the leader will restrain the stability of the traffic flow and prolong the time for the unstable traffic flow to stabilize.

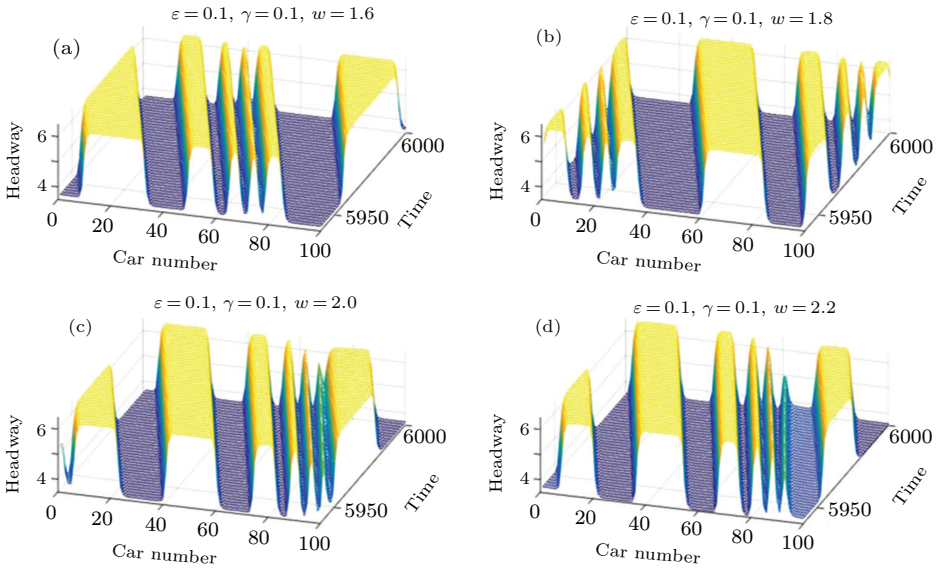


Fig. 7. Space–time evolution of the headway from with the $t = 5000$ s to 6000 s.

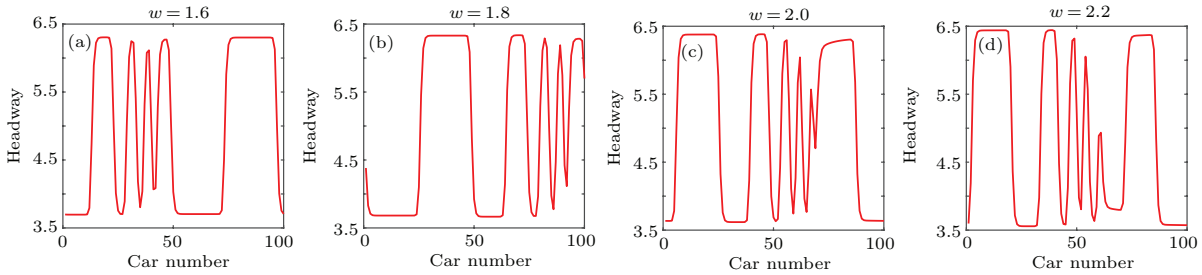


Fig. 8. Headway profiles of the density wave at $t = 6000$ s correspond to Fig. 6 respectively.

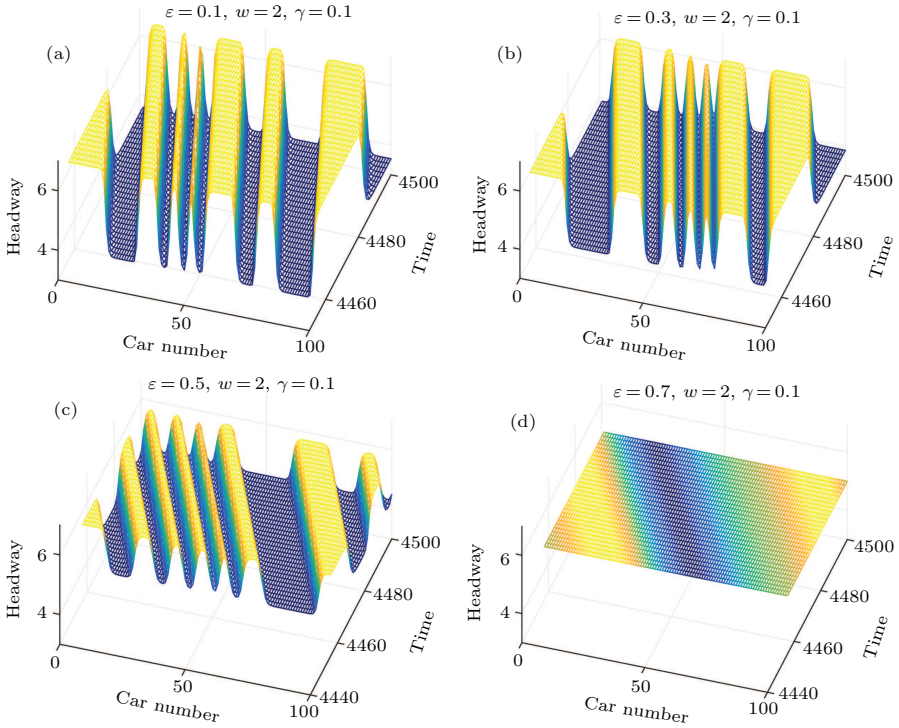


Fig. 9. Space–time evolution of the headway from with the $t = 4400$ s to 4500 s.

In Fig. 9, we explore the effect of the anticipated time on the stability of traffic flow in the improved car following model through a series of simulations, where Figs. 9(a)–9(d) correspond to ε ($\varepsilon = 0.1, 0.3, 0.5, 0.7$), respectively. It can be obviously seen from the change curvature in Fig. 8 that considering the anticipated time contributes to stable movement of the system. Specially, when $\varepsilon = 0.7\ \mathrm{s}^{-1}$, the density wave change curvature is zero, at this time, the traffic flow steadily travels with a constant headway, and the entire traffic flow system has the highest stability. Therefore, we conclude that considering the driving characteristics of subject driver can effectively improve the stability of the traffic flow. The proposed new model considers the anticipated time and the subject driver uses the received original traffic information combines with his own prediction of the front traffic state to shorten the time responds to the front traffic situation, which provides a comprehensive improvement to the entire car-following behavior.

Figure 10 displays the headway profiles and density waves for anticipated time at $t = 4500$ s corresponding to panels in Fig. 8 respectively. From Figs. 10(a)–10(d), considering the speed difference, the traffic congestion conditions can be effectively alleviated, and as the anticipated time increases, the amplitude of the density wave gradually decreases, which means the traffic flow tends to move with a stable headway. The improved model has improved to a greater extent in eliminating interference. From Fig. 10, we obtain that parameter ε can promote the stability of traffic flow.

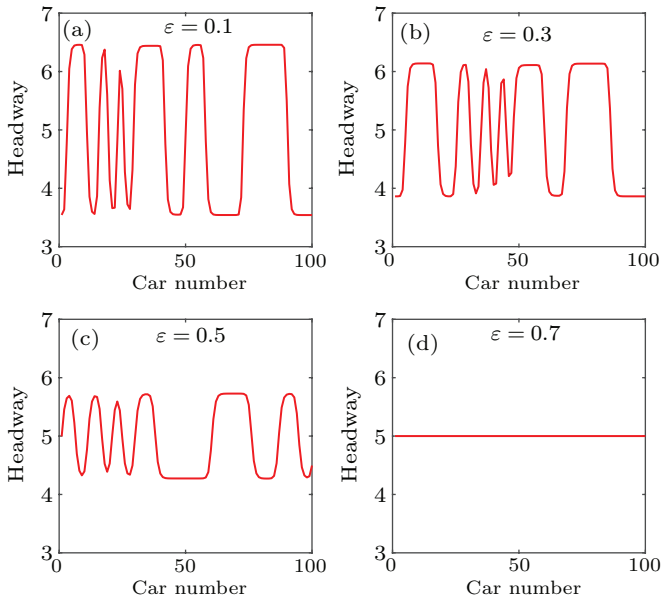


Fig. 10. Headway profiles of the density wave at $t = 4500$ s correspond to Fig. 8 respectively.

Figure 11 mainly depicts the hysteresis loop relationships between the velocity and density, which are shown with deferent γ ($\gamma = 0.05$, 0.1, 0.15, 0.2) respectively. As we can see the size of the loop gradually decrease with the value increases γ in Fig. 11. This also means that considering driver's stabilizing driving behavior can effectively ease traffic congestion and promote the stability of the system at the same time.

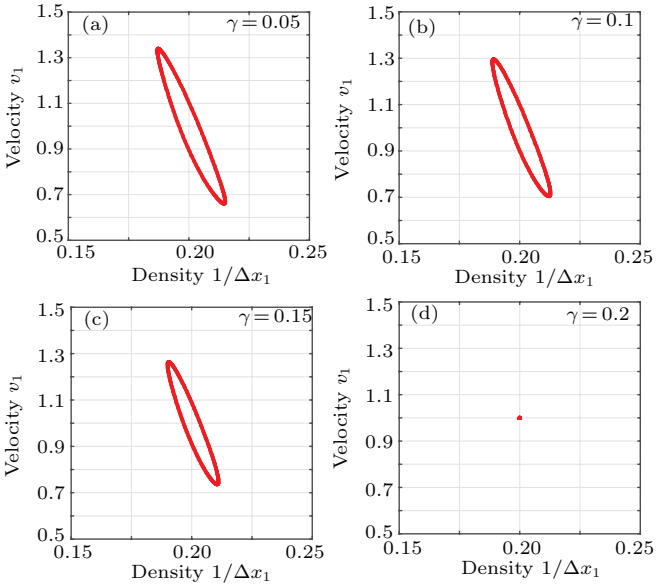


Fig. 11. The hysteresis loops relations of the velocities $v_1(t)$ and the density $\rho_1(t) = 1/\Delta x_1(t)$ respectively.

8. Conclusion

In this paper, we take the anticipated time and stabilizing driving behavior into the visual angle model, combining anticipated time with stabilizing driving behavior to explore driver's sensitivity of change of angle information. The relationship of neutral stability is obtained by linear stability analysis. Meanwhile, bifurcation analysis for the improved car-following model considering the visual angle, anticipated time and stabilizing driving behavior is investigated. Hopf bifurcation analysis mainly consists of two modules, one is theoretical analysis and the other is numerical simulation. Through the Hopf bifurcation analysis we can obtain the critical points. Results show that bifurcation analysis results are highly coincide with the stability condition of linear stability analysis. Furthermore, from the three-dimensional bifurcation diagram, it is found that the critical points of Hopf bifurcation are located on the boundary between the stability region and the instability region. Hopf bifurcation leads to conversion of stable traffic flow to irregular traffic flow. In addition, the TDGL equation is obtained by nonlinear analysis, and then the coexistence curve, metastable curve and critical point are described according to the obtained thermodynamic potential. We obtain the mKdV equation of the model in the same way. Finally, the parameter calibration and numerical simulation results display that the anticipated time and stabilizing driving behavior both play a positive role on traffic flow, which is opposite to the visual angle. Based on the conclusions, the article will make contributions on providing theoretical support for the establishment of intelligent transportation systems and references for traffic management systems.

Acknowledgements

Project supported by the Natural Science Foundation of Zhejiang Province, China (Grant Nos. LY22G010001, LY20G010004), the Program of Humanities and Social Science of Education Ministry of China (Grant No. 20YJA630008), the National Key Research and Development Program of China-Traffic Modeling, Surveillance and Control with Connected & Automated Vehicles (Grant No. 2017YFE9134700), and the K.C. Wong Magna Fund in Ningbo University, China.

References

[1] Sun Y Q, Ge H X and Cheng R J 2019 *Phys. A* **521** 752
[2] Ge H X, Dai S Q, Dong L Y and Xue Y 2004 *Phys. Rev. E* **70** 066134
[3] Jiang C T, Ge H X and Cheng R J 2019 *Phys. A* **513** 465
[4] Tian H H, Xue Y, Kan S J and Jiang Y J 2009 *Acta Phys. Sin.* **58** 4506 (in Chinese)
[5] Nagatani T 1996 *J. Phys. Soc. Jpn.* **65** 3150
[6] Redhu P and Gupta A K 2015 *Commun. Nonlinear Sci. Numer. Simul.* **27** 263
[7] Chang Y Y and Cheng R J 2019 *Physica A* **531** 12175
[8] Cheng R J, Ge H X and Wang J F 2018 *Appl. Math. Comput.* **332** 493
[9] Zhai Q T, Ge H X and Cheng R J 2018 *Phys. A* **490** 774
[10] Chandler R E, Herman R and Montroll W E 1958 *Operations Res.* **6** 165
[11] Gazis D C and Rothery H R W 1961 *Operations Res.* **9** 545
[12] Herman R, Montroll E W, Potts R B and Rothery R W 1959 *Operations Res.* **7** 86
[13] Yang Q I and Koutsopoulos H N 1996 *Transport. Res. C* **4** 113
[14] Edie L C 1961 *Operations Res.* **9** 66
[15] Greenshields B D, Bibbins J, Channing W and Miller H 1935 *Proceedings of the Highway Research*, December 6–7, 1935, Washington, U.S. p. 448
[16] Lee G 1966 *Operations Res.* **14** 595
[17] Jin Z Z, Cheng R J and Ge H X 2018 *Mod. Phys. Lett. B* **32** 1750366
[18] Newell G F 1961 *Operations Res.* **9** 209
[19] Helly W 1961 *Proceedings of the Symposium on the Theory of Traffic Flow* p. 207
[20] Koshi M, Kuwarara M and Akahane H 1992 *Ite J.* **62** 17
[21] Xing J 1995 *Proceedings of the Steps Forward Intelligent Transport Systems World Congress*, November 9–11, 1995, Yokohama, Japan, p. 1739
[22] Bando M, Hasebe K, Nakayama A, Shibata A and Sugiyama Y 1995 *Phys. Rev. E* **51** 1035
[23] Helbing D and Tilch B 1998 *Phys. Rev E* **58** 133
[24] Jiang R, Wu Q and Zhu Z 2001 *Phys. Rev. E* **64** 017101
[25] Yan C Y, Ge H X and Cheng R J 2019 *Phys. A* **535** 122216
[26] Michaels R M 1963 *Proceedings of the Second International Symposium on the Theory of Traffic Flow* 1963, Paris, OECD, p. 44
[27] Winsum W V 1999 *Transportation Research Part F-Traffic Psychology and Behaviour* **2** 207
[28] Andersen G J and Sauer C W 2007 *The Journal of the Human Factors and Ergonomics Society* **49** 878
[29] Jin S, Wang D H, Huang Z Y and Tao P F 2011 *Phys. A* **390** 1931
[30] Huilgol R R 1978 *Quart. Appl. Math.* **36** 85
[31] Igarashi Y, Itoh K, Nakanishi K, Ogura K and Yokokawa K 1999 *Phys. Rev. Lett.* **83** 718
[32] Orosz G, Wilson R E and Krauskopf B 2004 *Phys. Rev. E* **70** 026207
[33] Yamamoto M, Nomura Y and Sugiyama Y 2009 *Phys. Rev. E* **80** 026203
[34] Gasser I, Sirito G and Werner B 2004 *Physica D* **197** 222
[35] Jin Y F and Xu M 2010 *Chin. Phys. Lett.* **27** 040501
[36] Zhang Y C, Xue Y, Zhang P, Fan D L and He H D 2019 *Phys. A* **514** 133
[37] Ossen S, Hoogendoorn S P and Gorte B G H 2006 *Transportation Research Record Journal of the Transportation Research Board* **1965** 121